Sensors and Materials, Vol. 38, No. 4 (2026) 1751–1767
MYU Tokyo

S & M 4404

Image Reconstruction for Electromagnetic Tomography Based on Improved Cuckoo Search Algorithm

Ying Wang,[1*] Xianglong Liu,[2] and Yue Yang[1]

[1]School of Mechanical and Electrical Engineering, Zhengzhou University of Technology, Zhengzhou 450044, China
[2]School of Electrical and Information Engineering, Zhengzhou University of Light Industry, Zhengzhou 450002, China

(Received December 11, 2025; accepted February 26, 2026)

Keywords: electromagnetic tomography (EMT), inverse problem, Cuckoo Search, imaging algorithm

Electromagnetic tomography (EMT) is a promising and flexible technique for imaging conductivity and/or permeability because of its noncontact nature. However, the EMT inverse problem is both ill-posed and ill-conditioned because of the soft-field nature of the electromagnetic field and the limited prior information, which significantly impacts imaging quality. To overcome this challenge, an improved Cuckoo Search algorithm is introduced, incorporating a dynamic adaptive mechanism to adjust the discovery probability P_α and adaptive step size α. This modification improves the search capability, leading to higher optimization accuracy and faster convergence. Numerical simulations demonstrate that the proposed algorithm outperforms other classical techniques, particularly in terms of typical conductivity distributions. Further validation using the developed modular EMT system confirms the superior imaging performance of the method, making it a promising candidate for practical EMT applications.

1. Introduction

Electromagnetic tomography (EMT) is an imaging method, which aims to reconstruct the internal conductivity and/or permeability distribution from boundary voltage measurements.[1,2] EMT is attractive in industrial and medical fields, such as nondestructive testing,[3] foreign object detection,[4–6] multiphase flow measurement,[7,8] and intracranial hemorrhage detection,[9–11] owing to its characteristic of being contactless and fast.

Owing to the ill-posed nature of the EMT inverse problem, image reconstruction remains a significant challenge.[12] Researchers have proposed various algorithms to address these reconstruction issues. Currently, EMT image reconstruction approaches are mainly classified into noniterative and iterative methods.[13] Noniterative methods, such as linear back projection (LBP), Tikhonov regularization (TR), and truncated singular value decomposition (TSVD), are commonly used for online imaging. However, these methods often produce low-quality reconstructions when applied to complex phantom objects. On the other hand, iterative methods

*Corresponding author: e-mail: jyjdle@163.com
https://doi.org/10.18494/SAM5816

ISSN 0914-4935

include the Landweber iteration, conjugate gradient (CG) algorithm, algebraic reconstruction technique (ART) algorithm, simultaneous iterative reconstruction technique (SIRT) algorithm, iterative TR, and Cuckoo Search. The Landweber method, based on steepest descent, solves the inverse problem using the first derivative and enhances convergence with a projected operator.[14] The CG method, a powerful global search technique, efficiently solves sparse linear equations using conjugate directions, overcoming the limitations of both steepest descent and Newton's method. ART and SIRT, often used in CT imaging, differ in how they update the distribution vector during iterations. ART updates the vector using a single set of measurements per iteration, which can lead to nonconvergence due to measurement outliers. In contrast, SIRT uses more information to improve convergence, although both ART and SIRT require multiple iterations to produce satisfactory results.[15]

Cuckoo Search is a swarm intelligence optimization algorithm proposed by Yang of Cambridge University.[16] It is also a new meta-heuristic search algorithm. The idea is mainly based on two strategies: the nest parasitism of cuckoos and the Lévy flights mechanism. By searching for an optimal bird's nest by random walk to hatch their own eggs, this method can achieve an efficient optimization mode.[17] The main advantages of the Cuckoo Search algorithm are less parameters, simple operation, easy implementation, random search path optimization, and strong optimization ability. Tian *et al.* found that the choice of probability P will affect the search of the optimal solution: if P is very large, the better solution is difficult to converge to the optimal solution; if P is very small, it will make the current poor solution converge slowly.[18] Therefore, the dynamic discovery probability is introduced to optimize the performance of the improved Cuckoo Search algorithm.[18] In Ref. 19, by changing the discovery probability, the dynamic adaptive mechanism was used to control the discovery probability P to improve the search ability and accelerate the convergence speed. In Ref. 20, it is considered that the Levy flight mode lacks adaptability. To adjust the interval between large and small steps adaptively and coordinate the relationship between optimization accuracy and global optimization ability, an adaptive dynamic adjustment step size strategy based on the best bird's nest position is proposed. Qin *et al.* improved the information step size of the dominant solution exchange to strengthen the local search ability and make its advantages complementary.[21] The experimental results show that it can quickly converge to the global optimum in high dimension. Andrew used an improved version based on population sorting to guide the step size of random walk. The results showed that the improved algorithm is superior to the standard Cuckoo Search algorithm.[22] Wang *et al.* introduced an adaptive mechanism, which combines the adaptive discovery probability with the adaptive step length and also improves the optimal solution of the algorithm.[23]

In this paper, we first briefly introduce the basic principles of EMT, including forward problem, inverse problem, and sensitivity matrix. Then, on the basis of introducing the basic principle of the Cuckoo Search algorithm, an improved Cuckoo Search image reconstruction algorithm is proposed to improve the search ability and accelerate the convergence speed. Finally, simulations and experiments involving various phantom objects are conducted to confirm the effectiveness of the proposed algorithm.

2. Basic Principle of EMT

The EMT problem-solving fundamentally comprises both forward and inverse problem formulations.[24] The boundary voltage measurements are obtained through the computational resolution of the electromagnetic tomography forward problem, given a priori knowledge of the electrical conductivity distribution within the imaging targets.[25] Numerical simulations employ finite-element-method-based computational frameworks to address the forward problem, while experimental setups resolve it through the direct measurement of induced voltages via electrode arrays. The EMT inverse problem focuses on reconstructing the internal conductivity distribution or material characteristics of inspected objects by applying optimized image reconstruction algorithms to measured induced voltage data.[26]

2.1 Forward problem of EMT

The EMT fundamentally operates through dual theoretical frameworks: the forward problem and the inverse problem. The forward problem involves the modeling of electromagnetic field interactions to predict sensor-induced voltage signals between excitation and detection coils, given predefined conductivity and permeability distributions within the imaging domain. The EMT satisfies Maxwell's equations, as shown in Eq. (1).

$$\begin{cases} \nabla \times H = \sigma E + j\omega\varepsilon E + J_s \\ \nabla \times E = -j\omega B \\ \nabla \cdot B = 0 \\ \nabla \cdot D = 0 \end{cases} \tag{1}$$

Here, H represents the magnetic field intensity, E refers to the electric field intensity, B represents the magnetic flux density, D is the electric displacement, J_s denotes the applied source current density, ω represents the angular frequency, ε refers to the permittivity, and σ is the conductivity. Because the material has linear and isotropic properties in the imaging region, the following constitutive equations are satisfied:

$$B = \mu H, D = \varepsilon E, J = \sigma E\,, \tag{2}$$

where μ represents the permeability and J refers to the current density.

The EMT forward problem is solved by introducing the magnetic vector potential A, which conforms to $B = \nabla \times A$. In addition, it satisfies $E = -j\omega A$ in the time-harmonic electromagnetic field. The governing equation of the EMT forward problem can be written as

$$\frac{1}{\mu}\nabla^2 A - j\omega\sigma A = -J_s\,. \tag{3}$$

The matrix A can be determined by numerically solving Eq. (3) through the application of the finite element method. Additionally, the induced voltage U can be expressed as

$$U = -j\omega \oint A \cdot dl \,, \tag{4}$$

where $U \in R^M$, M represents the total count of voltage measurements, and dl signifies the line integral component.

2.2 Sensitivity matrix

The sensitivity matrix reflects subtle changes in induced voltage resulting from the alteration of the conductivity distribution. This matrix can be computed according to Geselowitz's sensitivity theorem, which is presented as

$$\frac{\partial V_{ij}}{\partial \sigma_k} = -\omega^2 \frac{\int_{\Omega_k} A_i \cdot A_j d\upsilon}{I_i I_j} \,, \tag{5}$$

where A_i and A_j serve as solvers for the forward problem when the the excitation coil i is excited by the current I_i and the detection coil j is excited by the current I_j. Ω_k represents the volume of perturbation. Figure 1 illustrates the spatial distributions of the sensitivity matrix, with the color gradient representing the relative sensitivity magnitude. The analysis reveals a pronounced sensitivity gradient across the imaging domain, where peripheral regions exhibit a significantly higher sensitivity than the central region. This spatial variation in sensitivity indicates that the objects positioned near the boundary exhibit superior reconstruction potential relative to those located in the central region.

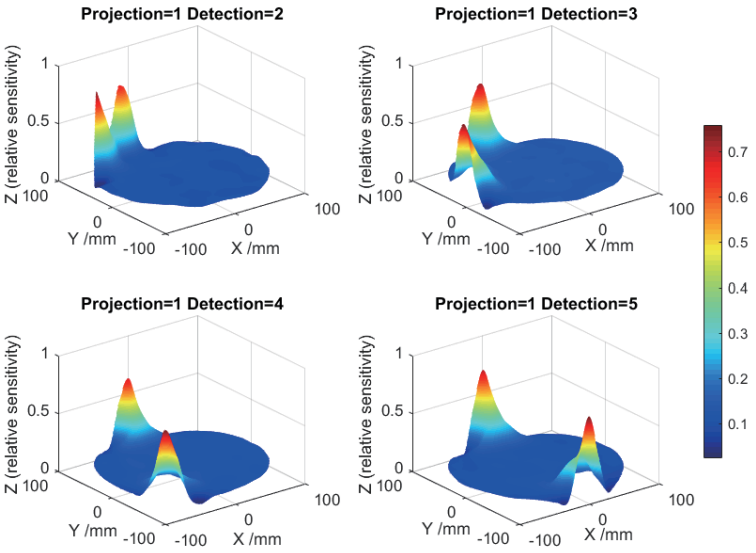

Fig. 1. (Color online) Sensitivity matrix distributions.

2.3 Inverse problem of EMT

The EMT inverse problem involves reconstructing the spatial conductivity profile within the imaging domain based on boundary voltage data. This reconstruction process is governed by a nonlinear functional relationship linking the measured voltages to the underlying conductivity distribution, mathematically expressed as

$$V_{ij} = \iint_D \sigma(x,y) F\left(x, y, \mu(x,y), \sigma(x,y)\right) dxdy \,, \tag{6}$$

where V_{ij} represents the induced voltage across coil pair *i*-*j*, F corresponds to the function describing the sensitivity field distribution, and D defines the cross-sectional area of the imaging domain. The relationship can be simplified and expressed as

$$V = F\left(\sigma\right). \tag{7}$$

To linearize the image reconstruction process, a truncated Taylor series expansion is applied, which is described as

$$V \approx F\left(\sigma_0\right) + \left.\frac{dF\left(\sigma\right)}{d\sigma}\right|_{\sigma_0} \left(\sigma - \sigma_0\right) + O\left(\left\|\sigma - \sigma_0\right\|^2\right). \tag{8}$$

The connection between the induced voltage U and the conductivity distribution g can be expressed in a linearized and discretized form, which is outlined as

$$U = Sg \,, \tag{9}$$

where S represents the sensitivity matrix.

The EMT inverse problem is inherently ill-posed and ill-conditioned, primarily because of the soft-field nature of the electromagnetic sensitivity field. Additionally, it is underdetermined, as the number of measurements is typically smaller than that of unknown gray values. Enhancing imaging quality holds significant potential for advancing the practical applications of EMT.

3. Cuckoo Search Algorithm

3.1 Basic principle of Cuckoo Search algorithm

The cuckoo bird practices brood parasitism, lacking the ability to incubate its own eggs. This compels it to locate suitable nests and depend on foster parents for the hatching and rearing of its offspring. Its reproductive strategy is primarily centered on the careful selection of hosts. During the breeding season, the cuckoo looks for hosts with matching hatching and brooding schedules,

similar chick-feeding behaviors, and eggs that resemble its own in shape and color, typically from *Passeriformes* species. Once a suitable host is identified, the cuckoo waits for the right moment—usually just before the host's eggs are set to hatch—and quickly lays its egg while the host is away foraging. In late spring and early summer, the cuckoo migrates north. It is incapable of building its own nest, hatching eggs, or raising its young. Each time it visits a nest, it lays only a single egg. Before laying its eggs, the cuckoo typically removes one or more of the host's eggs to avoid detection, ensuring the total number of eggs in the nest remains similar. Once the foster mother's chicks hatch, the cuckoo chicks instinctively push the host's eggs or chicks out of the nest, ensuring they are raised solely by the foster mother, which significantly boosts their chances of survival.

In natural environments, animals often exhibit random or semirandom patterns while foraging for food. According to Ref. 27, numerous flying species, including albatrosses and spider monkeys, display flight intervals that align with a power law distribution. The analysis of their flight trajectories (illustrated in Fig. 2) reveals that the occurrence of longer segments closely resembles the scale-free negative quadratic Lévy distribution, both demonstrating traits consistent with Lévy flight. Recent studies further indicate that similar Lévy-like behavior can be observed in human activities, as highlighted in Ref. 28.

Lévy flight represents a non-Gaussian stochastic process characterized by stationary increments that adhere to a Lévy stable distribution, with its step sizes conforming to a heavy-tailed Lévy stable distribution. This behavior involves frequent short-distance movements with smaller steps interspersed with occasional long-distance leaps. As illustrated in the Lévy flight trajectory, clusters of smaller jumps are distinctly separated by larger, more infrequent displacements.

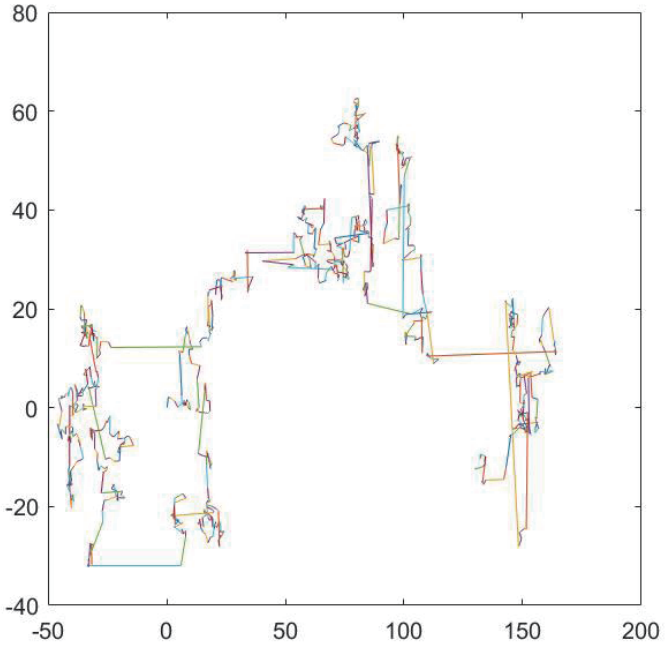

Fig. 2. (Color online) Simulated Levy flight trajectory.

Shlesinger incorporated this flight pattern into swarm intelligence search algorithms.[29] During the initial search phase, large steps are taken to explore and discover promising regions of the search space, which helps increase population diversity and expand the search range, thereby preventing the algorithm from getting trapped in local optima. In the later stages of the search, smaller steps allow the swarm to converge within a small range towards the global optimal solution. Li *et al.* applied this flight pattern to optimization algorithms and optimal search, demonstrating satisfactory results.[30] Doussot *et al.* proved that when the target positions exhibit random characteristics and are sparsely distributed without any regular pattern, Lévy flight is the most effective and ideal search strategy for M independent optimizers.[31]

Yang assumed the following three ideal conditions for the Cuckoo Search algorithm to simulate the nesting parasitic behavior of cuckoos.[16]

(1) Each cuckoo lays only one egg at a time and randomly selects one bird's nest storage.
(2) During the nesting process, the nest with the best eggs will be retained for the next generation.
(3) The number of available nests is fixed, and the probability of discovering foreign eggs in a nest is denoted as P, where $P \in [0, 1]$. If foreign eggs are discovered, the nest owner will build a new nest.

From the above three ideal conditions, the update formula for the position and path of the Cuckoo Search algorithm is

$$x_i^{(t+1)} = x_i^{(t)} + \alpha \oplus L(\lambda),\ i = 1, 2, \cdots, n, \tag{10}$$

where $x_i^{(t)}$ denotes the position of the i-th nest in the t-th generation. $\oplus$ represents point-to-point multiplication. α is the step size control quantity, which is used to control the search range of the step size, and its value obeys the normal distribution. $L(\lambda)$ is the Lévy random search path, and the random step size is Lévy distribution, that is, $L(\lambda) \sim t^{-\lambda}$, $(1 < \lambda \leq 3)$.

It can be seen from Eq. (10) that the walking mode is a random walk process. Owing to the random walk characteristics of Lévy flight, new solutions often appear near the local extremum point, so the short step search of Lévy flight is more conducive to improving the quality of the solution. In addition, there are also new solutions far away from the local optimal value, and the occasional large step exploration makes the algorithm not easy to fall into the local extreme point.[32]

The steps of the Cuckoo Search algorithm are as follows, based on the cuckoo bird's egg incubation process.

Step 1: Define the objective function $f(X)$, $X = (x_1, ..., x_d)^T$. The function is initialized, and the initial position X_i (i = 1, 2, ... , n) of n nests is randomly generated. The parameters such as population size, problem dimension, the maximum discovery probability P, and the maximum number of iterations are set.

Step 2: Select the fitness function and calculate the objective function value for each nest position to obtain the current optimal function value.

Step 3: Record the optimal function value of the previous generation and update the positions and states of the other nests using Eq. (10).

Step 4: Compare the current position function value with the optimal function value of the previous generation. If it is better, update the current optimal value.

Step 5: After updating the position, compare a random number $r \in [0,1]$ with P. If $r>P$, randomly change $x_i^{(t+1)}$; otherwise, keep it unchanged. Finally, retain the best nest position $y_i^{(t+1)}$.

Step 6: If the maximum number of iterations or the minimum error requirement has not been reached, return to step 2; otherwise, proceed to the next step.

Step 7: Output the global optimal position.

3.2 Improved Cuckoo Search image reconstruction algorithm

The parameters P_α, λ, and α in the Cuckoo Search algorithm play crucial roles in finding both globally and locally improved solutions. Specifically, P_α and α are key factors in fine-tuning the solution vectors and can also affect the algorithm's convergence rate. In the traditional Cuckoo Search algorithm, P_α and α are set to fixed values during initialization and remain unchanged throughout the generations. A major limitation of this approach is the number of iterations required to reach an optimal solution. When P_α is small and α is large, the algorithm's performance tends to degrade, resulting in a significant increase in the number of iterations. On the other hand, if P_α is large and α is small, the algorithm converges quickly but may fail to find the optimal solution.

The primary distinction between improved Cuckoo Search and Cuckoo Search lies in how P_α and α are adjusted. To enhance the performance of the Cuckoo Search algorithm and address the limitations caused by using fixed values for P_α and α, the improved Cuckoo Search algorithm employs variable P_α and α. During the early generations, P_α and α should be large enough to promote diversity in the solution vectors. However, in the later generations, these values are reduced to improve the fine-tuning of the solution vectors. The values of P_α and α change dynamically with each generation, as described by Eqs. (11)–(13), where NI represents the total number of iterations and i denotes the current iteration.

$$P_\alpha(i) = P_{\alpha max} - \frac{P_{\alpha max} - P_{\alpha min}}{NI} \times i \tag{11}$$

$$\alpha_i = \alpha_{min} + (\alpha_{max} - \alpha_{min}) d_i \tag{12}$$

$$d_i = \frac{\|n_i - n_{best}\|}{d_{max}} \tag{13}$$

Here, α_{max} and α_{min} denote the maximum and minimum step sizes, respectively. n_{best} is the best state of the current bird's nest position. n_i represents the location of the i-th nest; d_{max} is the maximum distance between the optimal location and the other nests.

4. Numerical Simulations and Experiments

4.1 Numerical simulations

Numerical simulations were conducted to assess the performance of the proposed algorithm for solving the multiple regularizers EMT imaging inverse problem. A series of simulations were carried out, and the results from the proposed algorithm were compared with those obtained from several traditional imaging methods, including LBP and TR. An EMT simulation model, consisting of 8 coils surrounding the imaging area, was created using an electromagnetic field analysis tool, as depicted in Fig. 3. The measured field has an inner radius of 100 mm. As shown in Fig. 3, the 8 coils are evenly distributed around the measured field. The reconstruction object is made of copper, while the background material, with low conductivity, is air.

FEM is utilized to address the forward problem. The excitation method for EMT simulation is a single coil, as described in Ref. 33. To assess different algorithms, five phantom objects were used. The mesh for the EMT inverse problem, depicted in Fig. 4, differs from the forward problem's mesh to prevent the inverse crime.

When a coil is selected as the excitation source, the magnetic field intensity distribution in the imaging area is illustrated in Fig. 5.

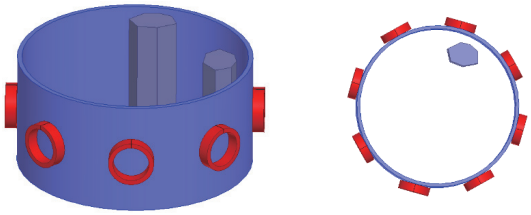

Fig. 3. (Color online) EMT simulation model with 8 coils.

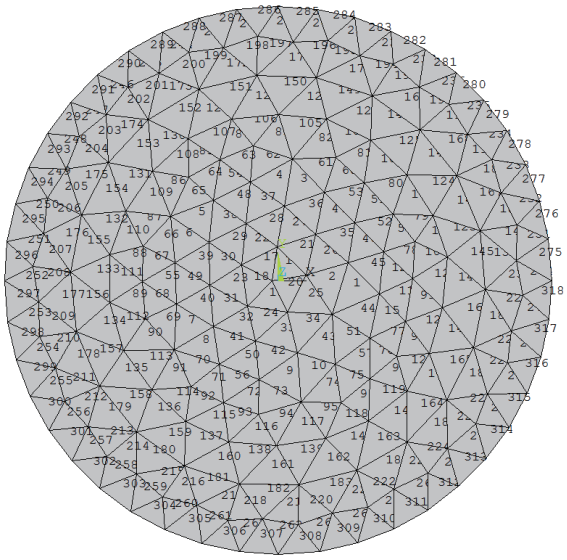

Fig. 4. (Color online) Mesh for the EMT inverse problem.

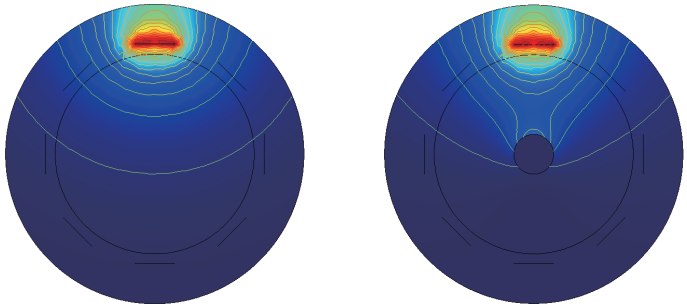

Fig. 5. (Color online) Magnetic field intensity distribution within the empty field (left) and object field (right).

LBP is a straightforward method, often used as an online reconstruction algorithm. However, for complex phantom objects, the quality of the reconstructed image is poor because the Moore–Penrose inverse of the sensitivity matrix is substituted with its transpose. LBP is defined as

$$g = S^T U \,. \tag{14}$$

TR is a commonly applied regularization technique across different fields. However, its use of L_2 regularization can lead to a smoothing effect, causing a loss of edge details in the reconstructed targets. It is represented as[34]

$$g = \left(S^T S + \mu I\right)^{-1} S^T U \,, \tag{15}$$

where μ represents the regularization parameter and I is the identity matrix.

The imaging accuracy is assessed using the image error (*IE*) and correlation coefficient (*CC*), defined as

$$IE = \frac{\left\|\hat{g} - g\right\|}{\left\|g\right\|}, \tag{19}$$

$$CC = \frac{\sum_{i=1}^{N}(\hat{g}_i - \overline{\hat{g}})(g_i - \overline{g})}{\sqrt{\sum_{i=1}^{N}(\hat{g}_i - \overline{\hat{g}})^2 \sum_{i=1}^{N}(g_i - \overline{g})^2}}, \tag{20}$$

where g and $\hat{g}$ represent the actual and reconstructed conductivity distributions, and $\overline{g}$ and $\overline{\hat{g}}$ denote the average values of g and $\hat{g}$, respectively. A lower *IE* and a higher *CC* indicate a better performance of the reconstruction algorithm.

Table 1 presents the results for LBP, TR, Cuckoo Search, and the proposed Adaptive Improved Cuckoo Search (AICS) algorithm. The regularization parameter for TR is chosen to be 0.05. For the proposed AICS method, its P_α is chosen using Eq. (11), and the step size is selected

Table 1
(Color online) Reconstructed results for the five phantom objects.

Typical pattern	LBP	TR algorithm	Cuckoo Search	IACS algorithm
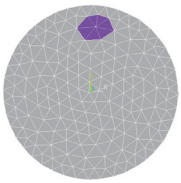	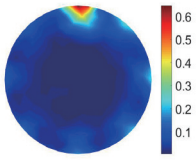	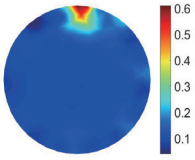	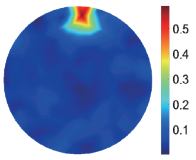	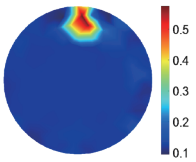
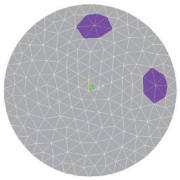	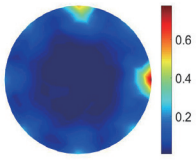	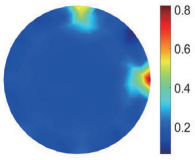	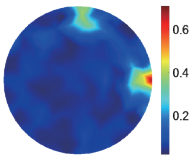	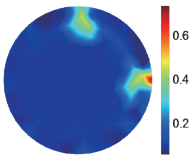
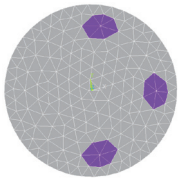	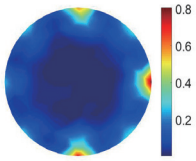	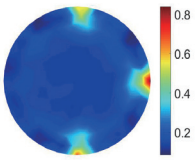	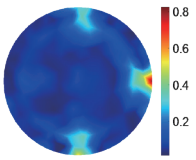	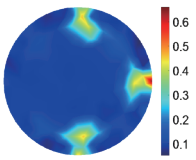
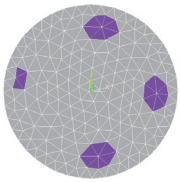	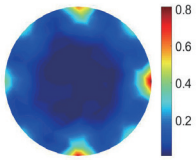	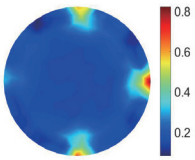	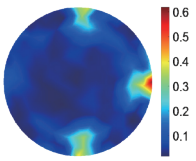	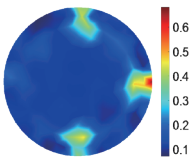
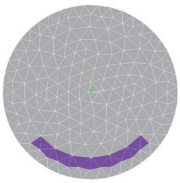	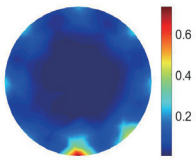	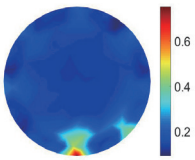	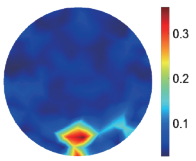	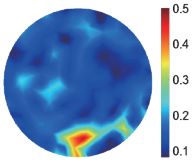

using Eq. (12). The first column of Table 1 shows the true distributions, with purple representing the high-conductivity medium and grey indicating the background material, namely, air. The remaining columns display the reconstruction results from the classical methods to the proposed AICS algorithm. Tables 2 and 3 present the *CC*s and *IE*s for various methods applied to the phantom objects.

Table 1 shows that the second column presents the results of reconstruction by LBP, which exhibits artifacts and distortions, particularly for complex phantom objects. The third column shows the results of reconstruction by TR, where reconstruction edges appear blurred owing to the smoothing effect. The fourth column presents the results of reconstruction by Cuckoo Search. The quality of the reconstructed images is enhanced compared with that obtained by the two previous noniterative algorithms, although it requires more computation time. The fifth column shows the results of reconstruction by the proposed AICS method. The reconstructed objects are correctly separated from the edges and align closely with the actual positions of the targets. These improved results demonstrate the effectiveness and advantages of the proposed

Table 2
Correlation coefficients.

Typical pattern	LBP	TR	Cuckoo Search	AICS method
1	0.2591	0.3890	0.4962	0.6743
2	0.2087	0.3560	0.4913	0.5258
3	0.2097	0.3762	0.4445	0.5589
4	0.1895	0.3472	0.4481	0.5019
5	0.0978	0.1977	0.2106	0.2518

Table 3
Image errors.

Typical pattern	LBP	TR	Cuckoo Search	AICS method
1	0.5228	0.5681	0.4554	0.4345
2	0.5158	0.5657	0.4380	0.4245
3	0.5099	0.5047	0.4415	0.4229
4	0.5111	0.5034	0.4298	0.4189
5	0.5197	0.5391	0.4795	0.4685

algorithm. From Tables 2 and 3, the *CC*s for the proposed algorithm are 0.6743, 0.5258, 0.5589, 0.5019, and 0.2518 for the five phantom objects, all of which are higher than those for the other image reconstruction algorithms. This provides further quantitative evidence of the superiority of the proposed algorithm. Additionally, the *IE*s for the proposed algorithm are smaller than those for the other algorithms, leading to the same conclusion. The numerical simulation results also indicate that simpler phantom objects are reconstructed more easily than complex ones among the five phantom objects. Under the same simulation conditions, the proposed AICS method reduces the average runtime from 12.16 to 9.70 s (approximately 20% improvement), demonstrating its fast convergence compared with that of the original Cuckoo Search algorithm.

4.2 Experimental results

To further verify the proposed algorithm, an experimental EMT system is developed in this study.[35] This system consists of an EMT sensor array, an excitation module, a detection module, a signal conditioning module, a lower computer (embedded controller), and a host computer. The hardware architecture of the EMT system is shown in Fig. 6.[36]

Figure 7 shows the experimental system, where Figs. 7(b) and 7(c) are the magnified views of the signal conditioning module and the O-shaped sensor array, respectively. In the EMT system, an 8-coil sensor generates a primary magnetic field and captures the induced voltages. A Tektronix AFG1022 provides the sinusoidal excitation signal, whereas an LT1210 amplifies the excitation signal to strengthen the magnetic field intensity. To amplify the weak induced voltages, a PGA AD8253 is used, allowing them to be acquired by the data acquisition module USB3200N. Two ADG406 chips manage the switching between the excitation and detection channels. The embedded controller, an STM32F103 microcontroller, processes signals from the host computer and controls the signal conditioning module. The host computer handles the imaging task, displaying the reconstructed results on the screen. The signal conditioning module is responsible for amplifying the excitation signal, boosting the detection signals, and switching

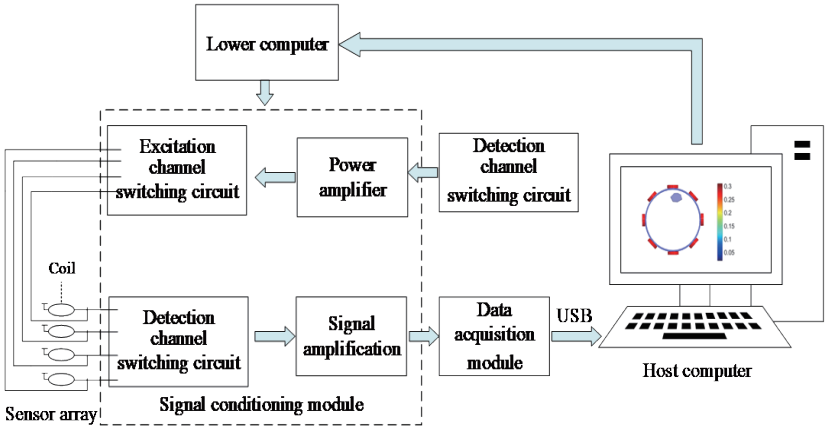

Fig. 6. (Color online) Hardware architecture of EMT system.

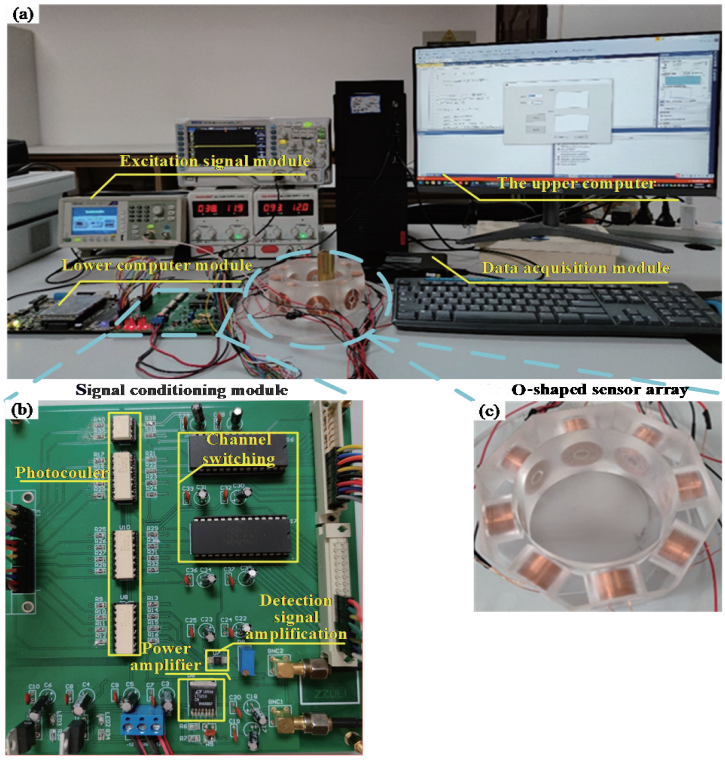

Fig. 7. (Color online) Photograph of the experimental system: (a) designed 8-coil EMT system, (b) signal conditioning module, and (c) O-shaped sensor array.

channels. It interfaces with both the embedded controller and the EMT sensor coils. This module is implemented via a PCB board designed by our team, with the detailed PCB layout available in Ref. 36.

Figure 8 illustrates the measurements for the fourth conductivity distribution. The U-shaped curves of the induced voltages in Fig. 8 align with the characteristics of the sensitivity matrix. The signal-to-noise ratio (SNR) of the EMT system is 48 dB.

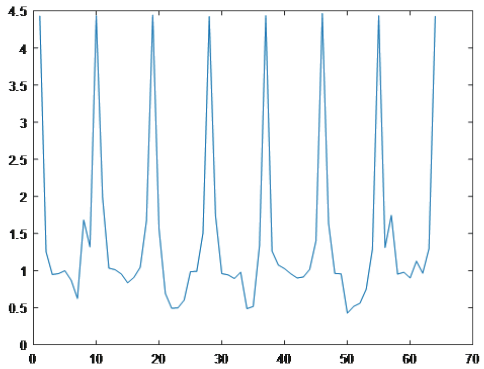

Fig. 8. (Color online) Measurements for the fourth conductivity distribution.

To assess the effectiveness of the proposed method, experiments are conducted using four typical conductivity distributions: one copper bar, two copper bars, three copper bars, and four copper bars. The copper bars represent a high-conductivity medium, while the surrounding gas serves as the low-conductivity background medium. Each copper bar has a diameter of 25 mm and a height of 100 mm. The conductivity of the meshed elements occupied by the copper bars is set to 1, while those not occupied by the bars are assigned a conductivity of 0. The true conductivity distributions of the objects are determined and used as the ground truth for evaluating the performance of different image reconstruction algorithms. LBP, TR, Cuckoo Search, and the proposed AICS method are employed to visualize the various conductivity distributions. The imaging tasks are performed on a host computer equipped with an Intel Core i5-8500 CPU and 16 GB of memory. The reconstruction results from the different algorithms are presented in Table 4, with the corresponding *CC*s for the reconstruction targets shown in Table 5. Table 6 shows the *IE*s for the four methods when applied to the phantom objects. In Table 4, the first column shows the actual conductivity distribution, whereas the subsequent columns display the reconstruction results from LBP, TR, Cuckoo Search, and the proposed AICS method.

Table 4 shows that classical imaging algorithms can accurately reconstruct the positions of the four types of phantom object, with clear separation between multiple target objects. Additionally, the number of imaging objects can be easily identified. However, determining the size of the imaging object remains challenging. The proposed algorithm, on the other hand, successfully reconstructs both the number and location of targets. Furthermore, as indicated by Tables 5 and 6, the *CC*s and *IE*s for the proposed AICS algorithm outperform those for the classical methods, demonstrating its superiority for reconstructing the four types of phantom object.

As shown in Tables 5 and 6, LBP yields the lowest *CC*s, indicating that it generates reconstructed images with significant distortions. This may be due to the approximation of the Moore–Penrose inverse of the sensitivity matrix. The *CC*s for TR are lower than those for both Cuckoo Search and the proposed AICS method, likely because of its excessive smoothing effect. On the other hand, Cuckoo Search produces higher *CC*s than LBP and TR, as it is an iterative algorithm. However, it is time-consuming and still suffers from artifacts owing to the absence of

Table 4
(Color online) Reconstructed images by the classical and proposed algorithm.

True distribution	LBP	TR method	Cuckoo Search	IACS method
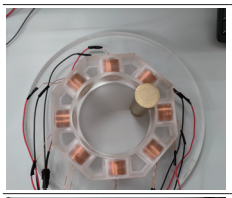	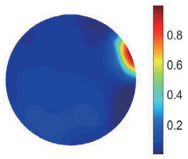	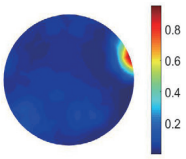	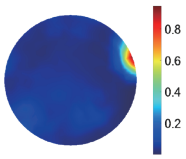	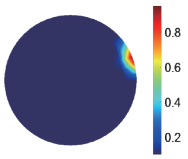
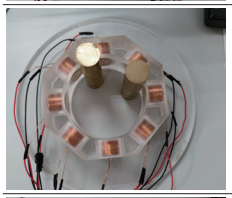	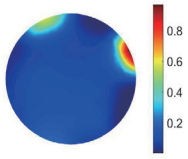	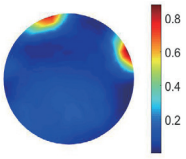	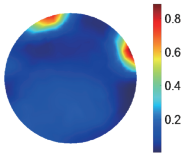	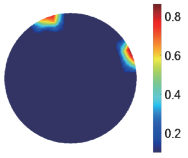
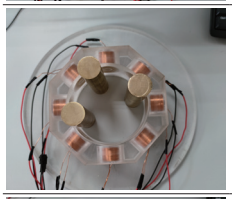	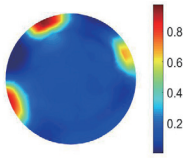	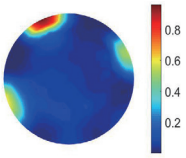	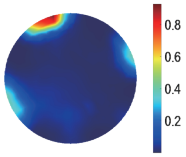	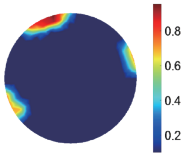
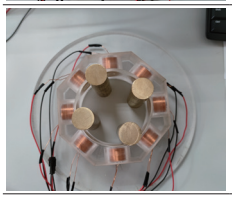	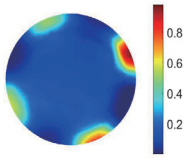	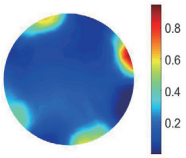	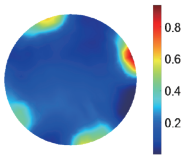	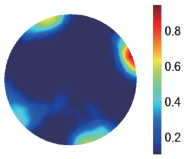

Table 5
Correlation coefficients of different image reconstruction methods for different distributions.

True distribution	LBP	TR method	Cuckoo Search	AICS method
1	0.6008	0.6816	0.6860	0.7113
2	0.5340	0.5701	0.5701	0.6450
3	0.5014	0.5225	0.5542	0.5994
4	0.3780	0.4288	0.4337	0.4526

Table 6
Image errors of different image reconstruction methods for different distributions.

True distribution	LBP	TR method	Cuckoo Search	AICS method
1	0.6421	0.4876	0.4826	0.4657
2	0.6548	0.5995	0.5972	0.5642
3	0.7433	0.5620	0.4605	0.4376
4	0.6905	0.6299	0.6238	0.5680

prior information on model deviations. The proposed AICS algorithm achieves the highest *CC*s for all four phantom objects, with values of 0.7113, 0.6450, 0.5994, and 0.4526. The *CC*s also show a decreasing trend as the complexity of the phantom object's distribution increases, further confirming that the reconstruction quality for a single target is superior to that for multiple imaging targets.

5. Conclusions

In this study, an improved Cuckoo Search algorithm is proposed by introducing a dynamic adaptive mechanism to control the discovery probability P_α and adaptive dynamic adjustment step size α. The modified algorithm improves the search ability because of its high optimization accuracy and convergence speed. Numerical simulations confirm that the proposed algorithm outperforms traditional imaging techniques when applied to typical phantom objects. The algorithm achieves the highest *CC*s, with values of 0.6743, 0.5258, 0.5589, 0.5019, and 0.2518 for the five phantom objects. The experiments conducted with our developed system further validate the effectiveness and imaging performance of the proposed algorithm. These results suggest that the algorithm holds significant potential for advancing EMT imaging and its practical applications.

Acknowledgments

This work was supported by the National Natural Science Foundation of China (Grant No. 62201511), Natural Science Foundation of Henan Province (No. 262300420402), Scientific and Technological Research Project in Henan Province (Nos. 262102240016 and 262102220070), and High-level Talent Research Start-up Funding Project (No. 23GC13). This work was also supported by the construct program of the key discipline in Zhengzhou University of Technology.

References

1 L. Ma and M. Soleimani: Meas. Sci. Technol. **28** (2017) 072001. https://doi.org/10.1088/1361-6501/aa7107
2 J. Feldkamp and S. Quirk: IEEE Sens. J. **21** (2021) 633. https://doi.org/10.1109/JSEN.2020.3014041
3 Z. Liu, W. Li, F. Xue, J. Xiafang, B. Bu, and Z. Yi: IEEE T. Magn. **51** (2015) 6201907. https://doi.org/10.1109/TMAG.2015.2430283
4 F. Li, J. F. P. J. Abascal, M. Desco, and M. Soleimani: IEEE Sens. J. **17** (2017) 976. https://doi.org/10.1109/JSEN.2016.2637411
5 W. Yin, G. Chen, L. Chen, and B. Wang: IEEE Sens. J. **11** (2011) 2233. https://doi.org/10.1109/JSEN.2011.2128866
6 W. Zhang, Q. Mo, P. Yan, and Y. Liu: IEEE T. Instrum. Meas. **70** (2021) 4507411. https://doi.org/10.1109/TIM.2021.3126394
7 Z. Chen, H. Hao, J. Salas-Avila, M. Fan, Y. Xie, S. Wang, J. Li, J. Xu, H. Wang, and W. Yin: Meas. Sci. Technol. **33** (2022) 074003. https://doi.org/10.1088/1361-6501/ac62aa
8 X. Ma, A. J. Peyton, R. Binns, and S. R. Higson: IEEE Sens. J. **5** (2005) 224. https://doi.org/10.1109/JSEN.2004.842443
9 Y. Chen, C. Tan, and F. Dong: IEEE T. Instrum. Meas. **71** (2022) 4501209. https://doi.org/10.1109/TIM.2021.3137539
10 Y. Jiao, T. Zhang, C. Fan, H. Cao, M. Chao, L. Han, W. Zhang, L. Mao, R. Liu, C. Xu, and L. Wang: Physiol. Meas. **44** (2023) 035012. https://doi.org/10.1088/1361-6579/acbeff
11 J. Xiang, Y. Dong, and Y. Yang: IEEE T. Med. Imaging **39** (2020) 4102. https://doi.org/10.1109/TMI.2020.3013100
12 X. Liu, Z. Liu, Y. Li, P. Zhao, and J. Wang: IEEE Sens. J. **20** (2020) 4758. https://doi.org/10.1109/JSEN.2020.2966274
13 X. Liu and Z. Liu: Flow Meas. Instrum. **65** (2019) 318. https://doi.org/10.1016/j.flowmeasinst.2019.01.010
14 W. Tian, J. Sun, M. Ramli, and W. Yang: IEEE Sens. J. **17** (2017) 7029. https://doi.org/10.1109/JSEN.2017.2749881
15 W. Yang and L. Peng: Meas. Sci. Technol. **14** (2003) R1. https://doi.org/10.1088/0957-0233/14/1/201
16 X. Yang: Proc. 2009 World Congr. Nature & Biologically Inspired Computing (NaBIC) (IEEE, 2009) 210. https://doi.org/10.1109/NABIC.2009.5393690

17 J. Chen, Z. Cai, H. Chen, X. Chen, J. E. Gutierrez, R. F. Mansour, and M. Ragab: J. Bionic Eng. **20** (2023) 2240. https://doi.org/10.1007/s42235-023-00365-7
18 X. Tian, B. Yang, X. Na, S. Cheng, L. Ba, and Y. Yuan: Chinese J. Phys. **95** (2025) 765. https://doi.org/10.1016/j.cjph.2025.03.039
19 J. Cheng, K. Tu, and Y. Xiong: Concurr. Comp-Pract. E. **37** (2025) 3639. https://doi.org/10.1002/cpe.70116
20 C. Ouyang, X. Liu, D. Zhu, Y. Li, J. Mao, C. Zhou, and J. Xue: Cluster Comput. **28** (2025) 68. https://doi.org/10.1007/s10586-024-04924-3
21 P. Qin, Y. Ding, Y. Li, B. Ye, Z. Gao, Y. Liu, Z. Cai, and H. Qi: Algorithms **18** (2025) 710. https://doi.org/10.3390/a18050262
22 W. Andrew: A nonrandom walk down wall street (Princeton University Press, 2011) pp. 263–268
23 D. Wang, J. Guan, H. Liu, H. Zhang, Q. Wang, L. Zhang, and J. Dong: Sustainability **17** (2025) 31. https://doi.org/10.3390/su17073206
24 Z. Cui, Y. Chen, and H. Wang: IEEE Sens. J. **19** (2019) 10016. https://doi.org/10.1109/JSEN.2019.2927629
25 Q. Wang, K. Li, R. Zhang, J. Wang, Y. Sun, X. Li, X. Duan, and H. Wang: Rev. Sci. Instrum. **90** (2019) 124703. https://doi.org/10.1063/1.5120118
26 J. Jeon, C. Park, S. Lee, H. Chae, J. Kim, and H. Son: IEEE T. Instrum. Meas. **71** (2022) 4502009. https://doi.org/10.1109/TIM.2022.3151951
27 J. Kang, J. Zhang, L. Chen, H. Zhang, and L. Zhuo: Appl. Intell. **55** (2025) 75. https://doi.org/10.1007/s10489-024-06017-5
28 H. Zhong, T. Liao, G. Fang, S. Zhang, and B. Zhou: J. Water Res. Plan. Man. **150** (2024) 04024016. https://doi.org/10.1061/JWRMD5.WRENG-6142
29 M. F. Shlesinger: Nature **443** (2006) 281. https://doi.org/10.1038/443281a
30 J. Li, Q. An, H. Lei, Q. Deng, and G. Wang: Mathematics **10** (2022) 2785. https://doi.org/10.3390/math10152785
31 C. Doussot, O. J. N. Bertrand, and M. Egelhaaf: PLOS Comput. Biol. **16** (2020) e1008272. https://doi.org/10.1371/journal.pcbi.1008272
32 H. Zhu, X. Qi, F. Chen, X. He, L. Chen, and Z. Zhang: Appl. Intell. **49** (2019) 791. https://doi.org/10.1007/s10489-018-1285-0
33 T. Zhang, W. Zhang, X. Liu, M. Dai, Q. Xuan, and X. Dong: IEEE T. Instrum. Meas. **71** (2022) 4005713. https://doi.org/10.1109/TIM.2022.3180406
34 M. Han, X. Cheng, and Y. Xue: Physiol. Measurement **37** (2016) 683. https://doi.org/10.1088/0967-3334/37/5/683
35 C. Tan, Y. Chen, Y. Wu, Z. Xiao, and F. Dong: IEEE T. Instrum. Meas. **70** (2021) 9508708. https://doi.org/10.1109/TIM.2021.3073439
36 X. Liu, Y. Wang, and D. Li: Rev. Sci. Instrum. **94** (2023) 034706. https://doi.org/10.1063/5.0126458